Stability and range of the type II $Bi_{1-x}W_xO_{1.5+1.5x}$ solid solution

Julia Wind[1*], Paula Kayser[1], Zhaoming Zhang[2], Ivana Radosavljevic Evans[3] and Chris D. Ling[1]

[1]*School of Chemistry, The University of Sydney, Sydney 2006, Australia*
[2]*Australian Nuclear Science and Technology Organisation, New Illawarra Road, Lucas Heights 2234, Australia*
[3]*Department of Chemistry, Durham University, South Road, Durham. DH1 3LE, UK*

[*]Corresponding author: jwin1641@uni.sydney.edu.au

Abstract

We have established the stability and range of the cubic type II phase of $Bi_{1-x}W_xO_{1.5+1.5x}$ using a combination of X-ray diffraction, neutron diffraction and X-ray absorption spectroscopy. Type II is a high temperature modification that can be obtained by quenching/rapid cooling of samples with compositions between x = 0.148 to x = 0.185. Slower cooling rates yield the stable low temperature polymorph, the tetragonal type Ib phase (Bi rich samples), and mixtures of type Ib and Aurivillius phase (W-rich samples). Throughout the entire solid solution range, type II exhibits a (3+3) dimensional incommensurate modulation with modulation vectors slightly smaller than 1/3 based on a cubic fluorite type subcell (δ-Bi_2O_3). The main structural motifs are well-defined tetrahedra of WO_6 octahedra in a δ-Bi_2O_3-matrix, with additional W being incorporated on corners and face centers of the approximate commensurate 3×3×3 supercell in octahedral coordination, confirmed by XANES analysis of the W L_3-edge. Impedance measurements reveal oxide ionic conductivities comparable to those of yttria-stabilised zirconia even after a decrease in ionic conductivity of about half an order of magnitude on thermal cycling due to transition to the tetragonal type Ib phase.

Keywords

Oxide ionic conductors; solid solution; bismuth oxide; incommensurately modulated structures; neutron diffraction; XANES

1. Introduction

The high temperature phase of Bi_2O_3, the so-called δ-phase, is the best oxide conductor known. However, its limited stability, between 729°C and its melting point at 817°C, prevents its commercial use as a solid oxide electrolyte. δ-Bi_2O_3 exhibits a simple cubic fluorite type

structure (space group $Fm\bar{3}m$, a = 5.66 Å) with 25% oxygen vacancies randomly distributed over the anion sublattice [1-3]. Great efforts have gone into stabilising the δ-Bi_2O_3 structure down to lower temperatures while maintaining large parts of its conductivity by doping with rare earths and higher valent transition metal cations such as Nb^{5+}, Ta^{5+}, Cr^{6+}, Mo^{6+} and W^{6+}. The competing effects of reducing the number of oxygen vacancies while simultaneously decreasing the coordination number of the introduced higher valent cations lead to a variety of fluorite-type δ-Bi_2O_3 related superstructures. Arguably the most interesting amongst these are the cubic 'type II' (3+3)-dimensional incommensurately modulated solid solution phases [4-10]. These phases are characterized by a series of three coupled modulations of the fluorite-type subcell $<\varepsilon\ 0\ 0>_f$.

We recently identified a new member of this class of (3+3)-dimensional incommensurately modulated phase, in the Bi_2O_3-W_2O_6 system [11]. $Bi_{1-x}W_xO_{1.5+1.5x}$ ($0.15 < x < 0.19$) has a modulation parameter ε = 0.321, i.e., very close to 1/3. This allowed us to solve the structure in a 3×3×3 commensurate approximate supercell of fluorite-type δ-Bi_2O_3 in the space group $F\bar{4}3m$ (a = 16.633 Å) by refinement against single-crystal Laue neutron diffraction data. The local chemistry is dominated by the transition from fluorite-type to pyrochlore-type with the main structural motif of W_4O_{18} tetrahedra of octahedra arising from the strong preference of W^{6+} for regular six-fold octahedral coordination environments.

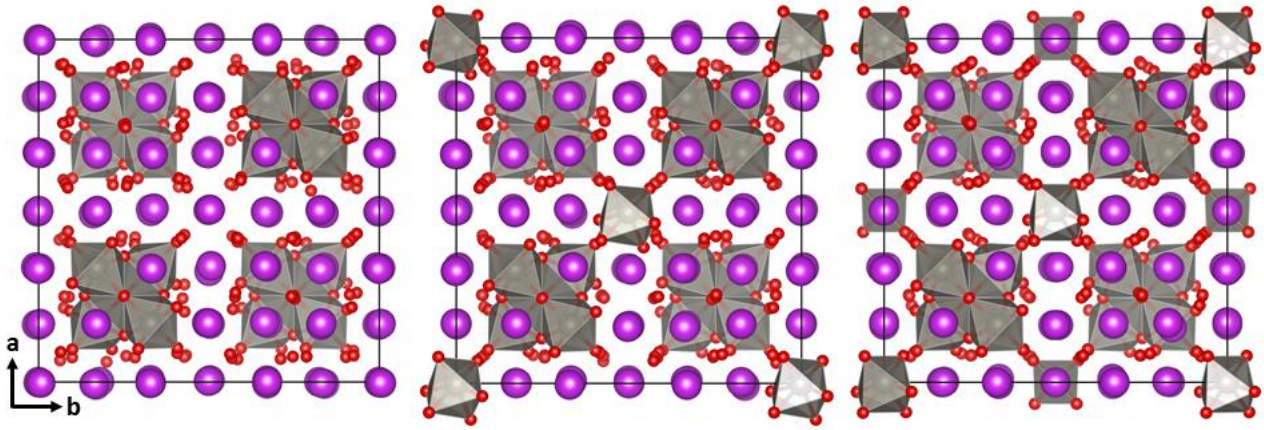

Figure 1: Crystal structures across the simulated type II solid solution range: $Bi_{23}W_4O_{46.5}$ (left); $Bi_{22.5}W_{4.5}O_{47.25}$ (middle) and $Bi_{22}W_5O_{48}$ (right). Bi atoms are purple, WO_6 polyhedra are grey, O atoms are red (reprint from Wind *et al.* [11]).

The obtained structure solution further suggested the presence of additional W on the Bi4 site (fcc site, positions at corners and face centers see Figure 1), resulting in a solid-solution range from $Bi_{22}W_4O_{46.5}$ to $Bi_{22}W_5O_{48}$ (i.e. x = 0.148 to x = 0.185; see Figure 1) in agreement with detailed *ab initio* (density functional theory, DFT) calculations that showed the structure adapts

very well to W^{6+}/Bi^{3+} substitution on the Bi4 site, while the W_4O_{18} clusters are a very stable configuration within the disordered δ-Bi_2O_3 matrix [11].

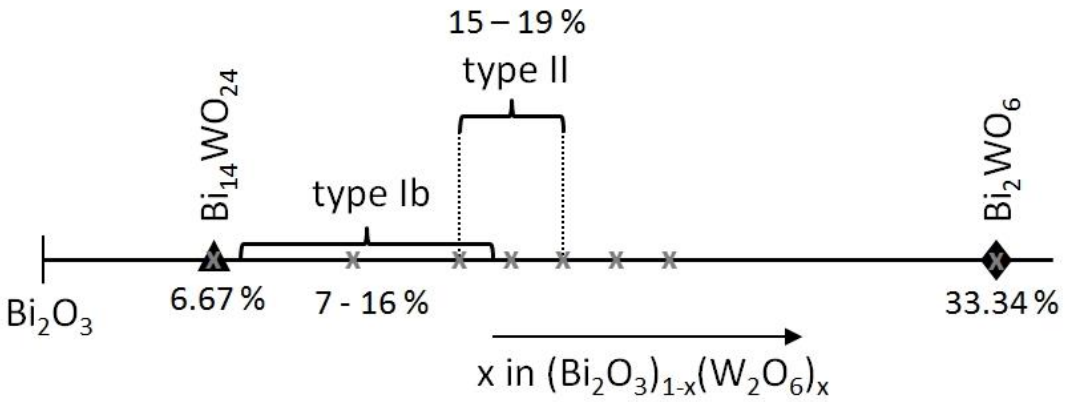

Figure 2: Partial phase diagram of the Bi rich side of the pseudo-binary Bi_2O_3-W_2O_6 system at room temperature, indicating the predicted compositional range for the high temperature type II modification. Crosses indicate sample compositions investigated in this work.

The partial phase diagram of the Bi-rich side of the pseudo-binary Bi_2O_3-W_2O_6 system at room temperature (Figure 2) shows a partial overlap of the reported hypothetical compositional region for the type II phase with the low-temperature tetragonal type Ib solid solution phase and the two-phase field formed by type Ib and Bi_2WO_6 phases. The type Ib phase has been intensively studied [12-16] and exhibits a rather complex tetragonal structure that is related to the fluorite δ-Bi_2O_3 subcell by $a = 2a_f + b_f$, $b = a_f + 2b_f$, $c = 2c_f$, i.e., a $\sqrt{5}\times\sqrt{5}\times2$ superstructure. The structure of the line phase Bi_2WO_6 is an n = 1 Aurivillius phase, composed of alternating perovskite- and fluorite-like layers [17,18].

In view of this, the aims of this work are to:

- Experimentally investigate the solid solution and stability range of the type II phase, which seems to overlap with compositional range of type Ib phase as well as with the type Ib + Aurivillius two phase field;
- Explore the relation between these phases;
- Experimentally investigate the local coordination environments via detailed X-ray absorption near edge structure (XANES) experiments; and
- Characterise the conductivity of this new high temperature polymorph compared to lower temperature phases and other transition metal doped bismuth oxides.

2. Experimental

2.1 Synthesis

Stoichiometric mixtures of WO_3 (99.999 %) and Bi_2O_3 (99.999%, preheated to 600°C for 5 h) were thoroughly ground with acetone in an agate mortar and pestle and preheated to 850°C for 5 h. The reground mixtures were then heated to 1000°C for another 5 h and furnace cooled to room temperature. Where necessary, another heating step was performed after which samples were quenched to room temperature by putting them onto a steel plate. Large samples (> 5 g) were ground together with ethanol in a planetary ball-mill followed by thorough regrinding in an agate mortar and pestle between individual heating steps.

Phase-pure samples were pressed into rods (0.7 cm diameter, 4-6 cm length) or pellets (diameter ~0.9 cm, ~0.1 cm thickness, density ~90 %) for variable temperature experiments and electrical characterisation respectively and sintered at 950°C for 5 h.

2.2 Data collection and analysis

Initial sample characterisation was done by room temperature powder X-ray diffraction on a Panalytical X'pert Pro diffractometer in Bragg-Brentano geometry using Cu Kα radiation.

Synchrotron X-ray powder diffraction (S-XRD) data were collected at the Powder Diffraction (PD) beamline of the Australian Synchrotron in Debye-Scherrer geometry using a Mythen microstrip detector [19]. Finely ground samples were packed into 0.1 mm diameter borosilicate glass capillaries for room temperature measurements. Data were collected at 21 keV (λ = 0.589263(3) Å, calibrated against a NIST LaB_6 standard) over the range $2° \leq 2\theta \leq 82°$. Variable temperature data (room temperature up to 950°C) were collected using the Anton Paar DHS 1100 furnace in flat plate geometry, with a heating and cooling rate of 10°C/min. Two diffraction patterns (2.5 min collection time each) were collected at each temperature to check for temperature equilibration. Neutron powder diffraction (NPD) experiments were carried out at the high-resolution diffractometer Echidna at the OPAL research reactor at ANSTO [20]. For room temperature measurements, 5-10 g samples were packed into 9 mm diameter vanadium cans. For variable temperature measurements (room temperature up to 950°C, heating and cooling rate 10°C/min, 10 min equilibration time), sample rods were suspended in a vacuum furnace using platinum wire. To check for sample equilibration, two NPD patterns were collected at each temperature step (30 min collection time each) and merged if no change occurred. Refinements against these data were carried out using the Rietveld method as

implemented in GSAS with the EXPGUI graphical interface [21]. Le Bail profile fits were performed using Jana [22].

AC impedance spectroscopy measurements were performed on a Solartron 1260 frequency response analyser over a frequency range of 10^{6}–10^{-1} Hz in air. The pellets were coated with a thin layer of platinum paste, mounted onto a Probostat A-6 cell. The pellet was then heated to 920°C for 1 h to burn out the organic components of the paste to form the platinum electrodes. Impedance data were collected on heating and cooling between 400 and 900°C in 60°C increments (heating and cooling rate of 10°C/min), allowing 40 min stabilisation time before each data collection. Impedance data were analysed using Zview 3.0a software.

High frequency intercepts were estimated as the total resistivities of the samples. To investigate the stability of these materials, three cycles of impedance measurements on heating and cooling were performed.

XANES spectra at the W L_3-edge were collected at the XAS beamline at the Australian Synchrotron [23]. Powder samples were diluted with cellulose powder (concentrations ~5000 ppm), sandwiched between Kapton tape and positioned in front of the X-ray beam. Measurements were performed at room temperature in fluorescence mode using a multi-element solid state Ge fluorescence detector. The energy scale was calibrated using the L_3 edge of a pure Pt foil (with the maximum in the first derivative set to 11562.8 eV). XANES spectra were analysed using the Athena software package [24].

3. Results and discussion

3.1 Room temperature structures

A total of six samples around the expected type II solid solution range with compositions between x = 0.04 ($Bi_{26}WO_{42}$) and x = 0.22 ($Bi_{21}W_6O_{49.5}$) were synthesised. In the following discussion, these samples will be referred to by using labels W1 to W6, corresponding to the number of tungsten atoms replacing Bi atoms within the 3×3×3 supercell, with a total number of 27 metal atoms. For samples between W4 ($Bi_{23}W_4O_{46.5}$) and W5 ($Bi_{22}W_5O_{48}$) (i.e., 14.8-18.5 at% W_2O_6) the cubic type II phase could be quenched to room temperature (Figure 3). These results are consistent with the solid solution range reported by Zhou *et al.* [15] and our recent computational study [11].

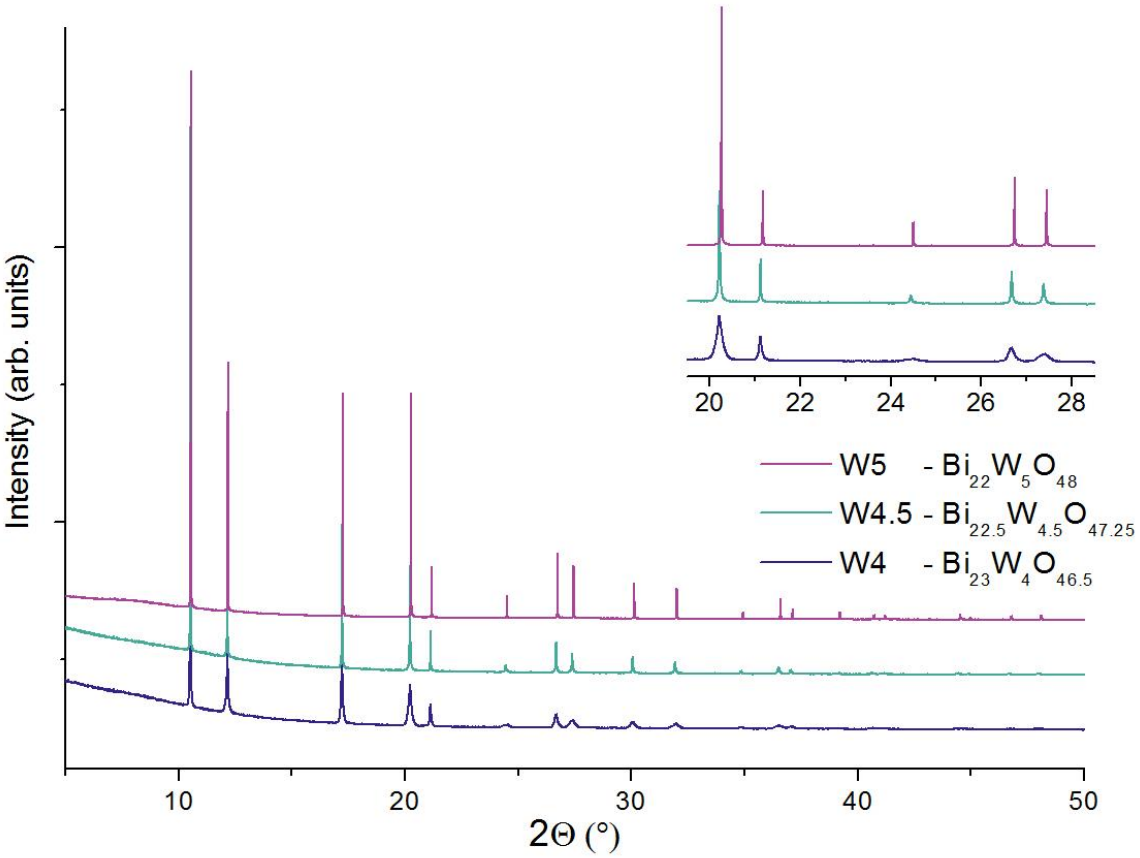

Figure 3: Synchrotron XRD patterns (λ = 0.589263(3) Å) from type II $Bi_{1-x}W_xO_{1.5+1.5x}$ solid solution samples, showing significant peak broadening for low W content.

At the bismuth-rich end (W4) there is just enough tungsten available to form the W_4O_{18} polyhedral cluster motif. Considerable strain exists in the structure due to the full occupation of Bi4/W site by large Bi^{3+} cations (cf. significant peak broadening in S-XRD patterns, see Figure 3). Similar peak broadening effects combined with an intensity decrease of the main first order superstructure reflection (000111) at the Bi-rich end of the type II compositional range has also been observed in the Bi_2O_3-Nb_2O_5 system [9]. Increasing the W content allows the structure to gradually relax until the Bi4/W site is fully occupied by W^{6+} cations, i.e., W5 which represents the W rich end of the type II solid solution. Lattice parameters were extracted from Rietveld refinements against S-XRD data (simple cubic fluorite type δ-Bi_2O_3 model [1]). Modulation vectors were extracted from combined Le Bail fits against NPD and S-XRD data, using a simple cubic fluorite type unit cell and three coupled modulation vectors (ε,0,0), (0,ε,0) and (0,0,ε). In the fitting procedure, the lattice parameter *a* was refined first. Subsequently, satellite reflections up to indices (*hkl*111) were included in order to extract the modulation vectors. The inclusion of higher order satellite reflections improved the fit but did not change the values obtained for ε. The average structure exhibits a (3+3)-dimensional incommensurate

modulation throughout the entire type II compositional range, with modulation vectors just smaller than 1/3, i.e., $0.3168(2) \leq \varepsilon \leq 0.3214(2)$. The superstructure can mainly be attributed to modulations in the oxygen sublattice. Due to the low X-ray scattering power of O compared to Bi and W, as well as the very low contrast between Bi and W, superstructure reflections in S-XRD patterns are very weak. Reasonable Rietveld refinements could therefore be obtained using only the simple cubic fluorite subcell, including mixed Bi/W occupancy on the Bi4 site (see Figure 4b). Lattice parameters *a* and modulation parameter ε both decrease with increasing tungsten content.

For samples outside of this narrow compositional range, the type II phase could not be quenched to room temperature. At the bismuth rich end (W1-W3), single phase samples with the tetragonal type Ib structure have been obtained. Samples with higher W content (W5.5 to W6) contain two phases – the tetragonal type Ib phase and the Bi_2WO_6 Aurivillius phase. Selected Rietveld refinements against S-XRD data are shown in Figure 4, refinement results are summarised in Table 1. For all refinements that include the type Ib phase, the structural model presented by Sharma *et al.* [12] in space group $I4_1$ was used.

Table 1: Structure type, unit cell parameters and Rietveld-refinement statistics for quenched $Bi_{1-x}W_xO_{1.5+1.5x}$ samples using S-XRD data. Modulation parameters were obtained by Le Bail profile fits against NPD data.

Composition	**Structure**	**lattice parameter**	**wRp**	**χ^2**	**ε**
$Bi_{24}W_3O_{45}$	tetragonal type Ib	*a* = 12.50184(4)	0.0370	3.186	
		c = 11.21643(6)			
$Bi_{23}W_4O_{46.5}$	cubic type II	*a* = 5.56888(2)	0.0344	2.753	0.3214(2)
$Bi_{22.5}W_{4.5}O_{47.25}$	cubic type II	*a* = 5.56661(1)	0.0339	2.492	0.3211(2)
$Bi_{22}W_5O_{48}$	cubic type II	*a* = 5.55355(1)	0.0355	3.540	0.3168(2)
$Bi_{21}W_6O_{49.5}$	orthorhombic	*a* = 5.45818(4)	0.0551	5.646	
	Aurivillius	*b* = 5.43759(4)			
	(32 w%)	*c* = 16.4301(2)			
	tetragonal type Ib	*a* = 12.4378(6)			
	(68 w%)	*c* = 11.10044(8)			

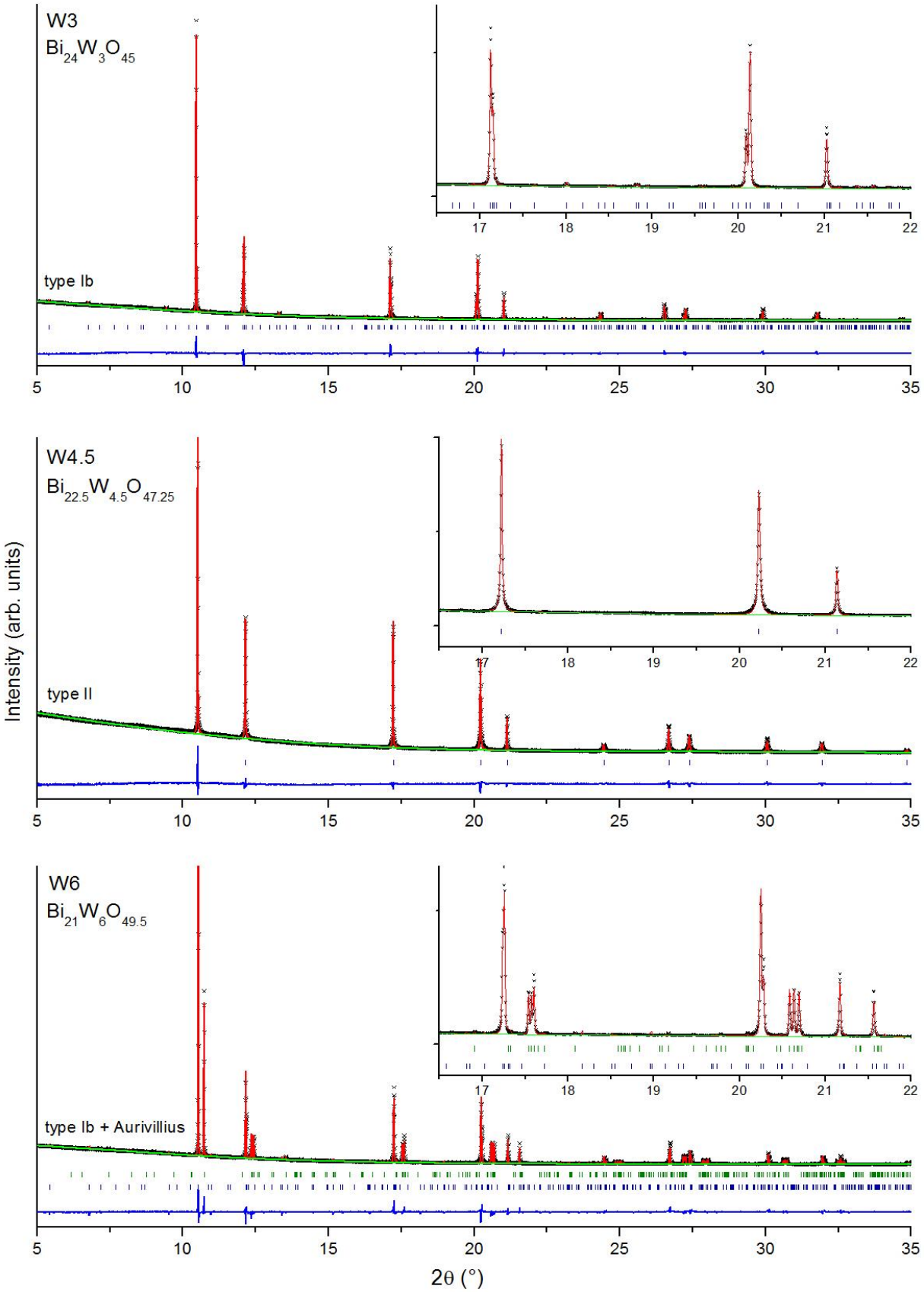

Figure 4: Rietveld refinements against S-XRD data across the solid solution range for quenched samples. Insets show smaller data ranges. Top: single phase sample showing exclusively type Ib structure; Middle: cubic fluorite type structure; Bottom: two phase sample with 68% type Ib (blue markers) and 32% Aurivillius phase.

Upon slow cooling (slower than quenching onto a steel plate), W4 samples yield exclusively tetragonal type Ib phase (a = 12.5346(2) Å, c = 11.2791(2) Å). Figure 5a shows an overlay of XRD patterns of the slow-cooled and quenched samples. Note the smaller volume per fluorite subcell of the quenched cubic phase (V_c = 173.64(1) Å^3) compared to the slow-cooled tetragonal phase (V_t = 177.21(7) Å^3), in agreement with our *in situ* variable temperature NPD data (see Section 3.2). The stability of the type II phase increases towards the W-rich end of the compositional range: for W5 samples, the type II phase could still be preserved down to room temperature applying cooling rates of 5°C/min or above. Slower cooling rates result in the formation of thermodynamically stable low-temperature two-phase mixtures of the Aurivillius and type Ib phases. This two-phase mixture is also obtained by annealing the sample at temperatures ≤ 850°C. Figure 5b shows the influence of different cooling rates on the structure of a sample with composition W5. These results are in perfect agreement with the currently accepted low-temperature phase diagram for the Bi_2O_3-W_2O_6 system (cf. Figure 2).

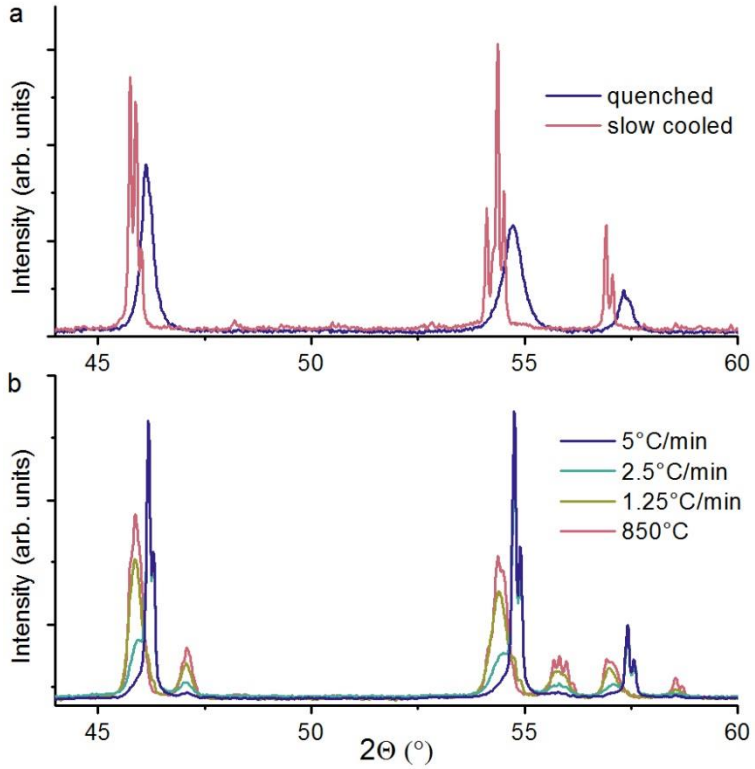

Figure 5: Excerpt of XRD patterns of samples with composition a) $Bi_{23}W_4O_{46.5}$ showing the tetragonal type Ib structure after slow cooling and the cubic type II structure after quenching. b) $Bi_{22}W_5O_{48}$ obtained using different cooling rates. Controlled cooling at 5°C/min yields exclusively the type II phase. Slower cooling rates (2.5 and 1.25°C/min) and annealing at temperatures ≤ 850°C results in two-phase mixtures of Aurivillius and type Ib.

3.2 Variable temperature studies

To investigate the relationship between the type Ib and type II phase, *in situ* variable temperature NPD (slow-cooled samples) and S-XRD (quenched samples) data were collected

for the end members of the solid solution range, i.e., W4 and W5, from room temperature up to 900-950°C. For W5, additional patterns were collected on cooling down to 700°C.

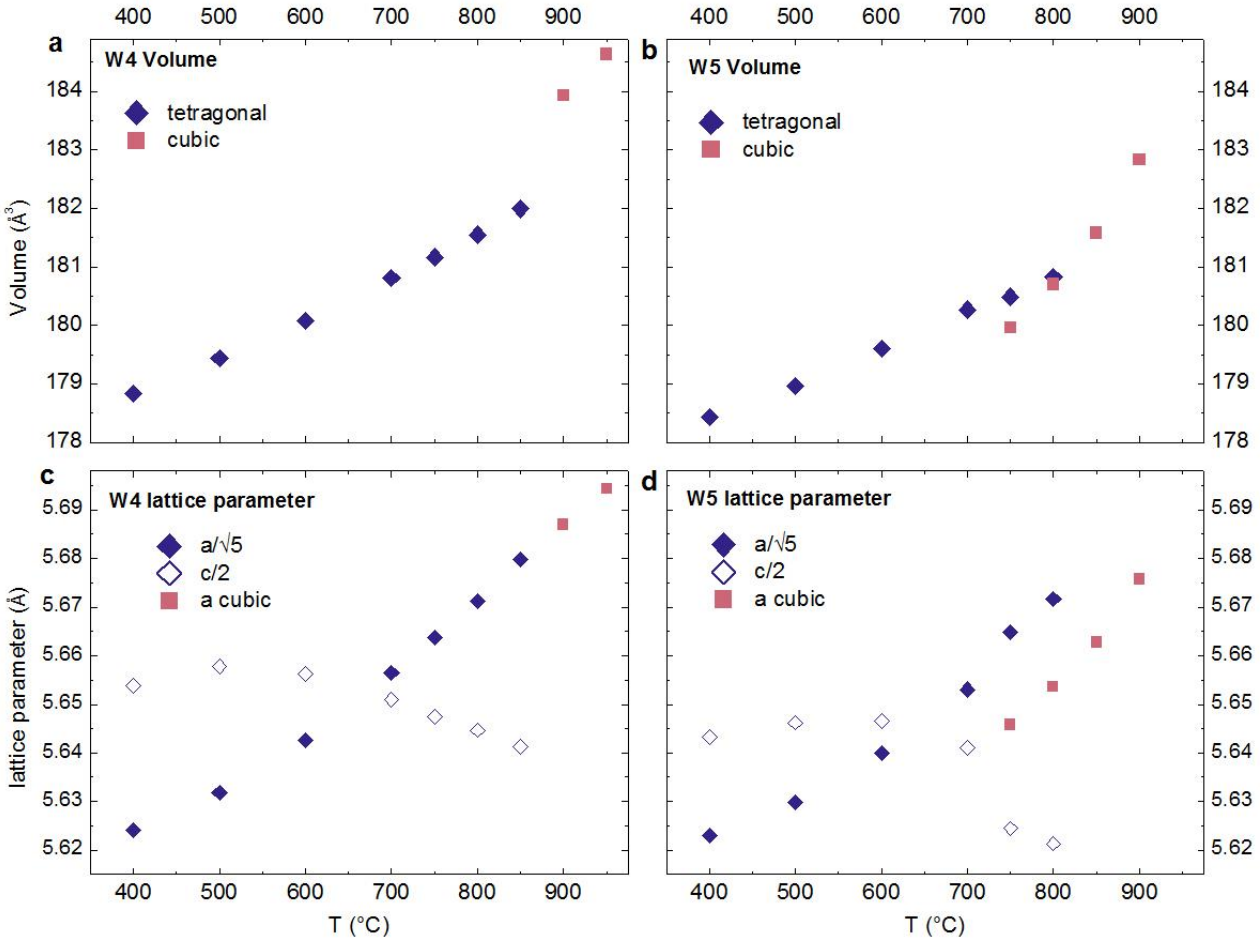

Figure 6: Volume (equivalent fluorite unit cell volume) and lattice parameters as a function of temperature extracted from Rietveld refinements against *in situ* variable temperature NPD data. Blue symbols indicate the tetragonal type Ib phase, red symbols the cubic fluorite type phase.

Sequential Rietveld refinements were carried out, allowing the refinement of lattice parameters, an overall temperature factor for metals and oxygen atoms respectively, and Lorentzian peak shape parameters and background terms at each temperature. Figure 6 shows the plot of the extracted unit cell parameters and unit cell volume (equivalent fluorite unit cell volume) as a function of temperature for the two samples (W4 and W5) extracted from NPD measurements. At lower temperatures, at the Bi-rich end (i.e., W4), the patterns could be fitted using the tetragonal type Ib model of Sharma et al. [12] (cf. slow cooled room temperature pattern presented in Section 3.1). While the unit cell volume increases almost linearly up to 850°C (blue data points in Figure 6a), there are clear changes of slope in the temperature trend for individual lattice constants *a* and *c* (cf. Figure 6c). Most notably, a contraction of the *c* axis is observed between 500 and 850°C (empty blue diamonds in Figure 6c), followed by an abrupt expansion of the *c* axis on transition to the cubic type II phase at ~900°C (red squares in Figure

6c). This sudden expansion of the *c* axis is accompanied by a significant jump in volume at the transition temperature. Above the transition, a simple cubic fluorite-type model was used for refinement.

The W5 sample exhibits two phases at lower temperatures: ~80% type Ib and ~20% Bi_2WO_6 Aurivillius phase (cf. section 3.1). On heating, the type Ib to type II phase transition occurs at ~850°C and is accompanied by a decrease in the amount of Aurivillius phase (<5% at 850°C). At 900°C, no Aurivillius phase was observed and the data could be fitted using a simple cubic fluorite-type model. On cooling, the cubic phase persists down to a temperature of 750°C at which it reverts back to type Ib + Aurivillius within about 1 h of equilibration time. Differences in refined lattice parameters obtained on heating and cooling were smaller than the symbols. Below the phase transition, behaviour of cell volume and lattice parameters are similar to the W4 sample, i.e., a linear increase in cell volume (blue diamonds in Figure 6b), a non-linear expansion in *a*-direction (solid blue diamonds in Figure 6d) and an initial expansion followed by a contraction in *c*-direction between 600 and 850°C (empty blue diamonds in Figure 6d). Contrary to the W4 sample, on transition to the type II phase no jump in volume is observed due to the expansion rate of the *c* axis being similar to the contraction rate of the *a* axis. After the transition to the cubic phase, the rate of expansion increases (change of slope in Figure 6b), resulting in a smaller volume of the super-cooled cubic phase compared to the tetragonal phase (red squares in Figure 6b).

This non-linear expansion/contraction behaviour in lattice parameters is further illustrated in excerpts of the synchrotron thermodiffractograms for quenched samples shown in Figure 7. On heating, the quenched type II phase persist up to a temperature of around 800-850°C at which point a first-order phase transition to tetragonal type Ib (and Aurivillius) phase occurs. Note that due to the experimental setup in the synchrotron data collection (flat plate geometry), the actual sample temperature (surface) was significantly lower than expected, thus the transition from tetragonal to cubic phase could not be observed during this experiment where the nominal upper temperature limit was 950°C. We estimate the actual sample temperature (at higher temperatures) to be approximately 50 °C below the measured temperature reading.

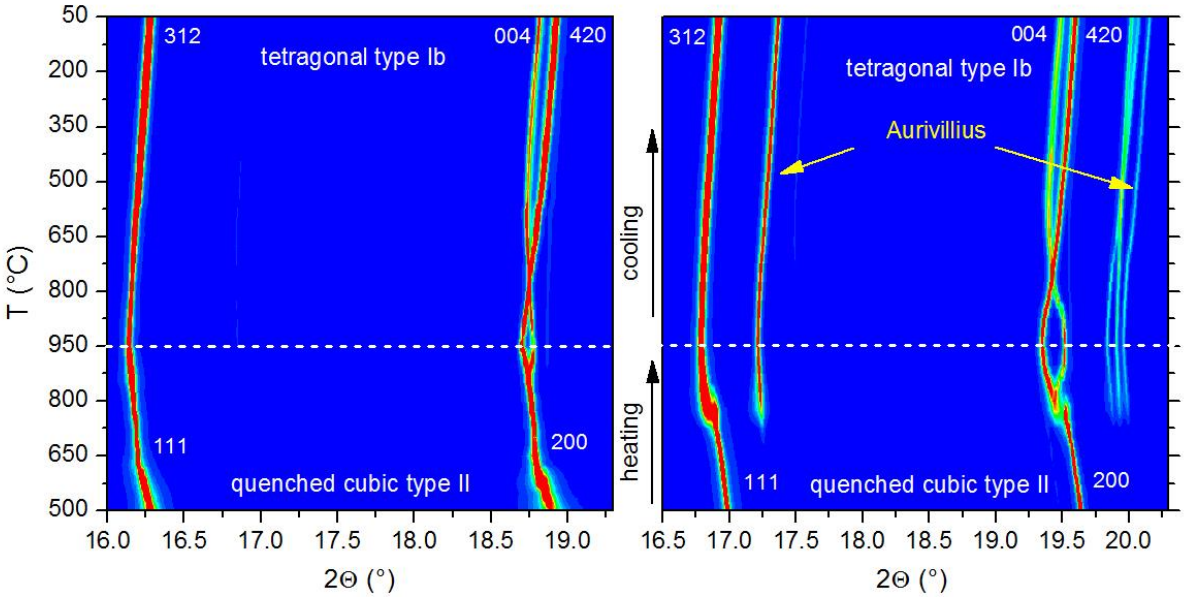

Figure 7: Excerpt of the thermodiffractograms (S-XRD data) for $Bi_{23}W_4O_{46.5}$ (left) and $Bi_{22}W_5O_{48}$ (right) showing the transition from the quenched type II phase to the tetragonal type Ib (and Aurivillius) phase on heating (lower part) and the anisotropic thermal expansion in the type Ib phase (upper part).

3.3 X-ray absorption near-edge structure (XANES) results

XANES is sensitive to the local structure around a specific element, providing information on the oxidation state, local coordination and site geometry [25,26]. Figure 8 shows the normalised W L_3 edge XANES spectra obtained from W3, W4, W4.5, W5 and W6 as well as the $Bi_{14}WO_{24}$ and Bi_2WO_6 standards, with their corresponding first derivatives plotted in the inset. The W^{6+} ions are coordinated to 4 and 6 oxygens in $Bi_{14}WO_{24}$ (i.e., tetrahedral environment [27,28]) and Bi_2WO_6 (i.e., octahedral environment [17,18]) respectively. W L_3-edge XANES spectra originate predominantly from the dipole transition of the W $2p_{3/2}$ core electrons into the empty 5d states in the conduction band, which is known to be sensitive to both the W oxidation state and its local coordination environment [29,30]. Figure 8 clearly shows that the W L_3-edge position of all the samples studied (W3, W4, W4.5, W5 and W6) is essentially the same as that of the two W^{6+} standards ($Bi_{14}WO_{24}$ and Bi_2WO_6), confirming the oxidation state W^{6+} in all samples. Although the main edge position of the two W^{6+} standards ($Bi_{14}WO_{24}$ and Bi_2WO_6) is practically the same, there are distinct differences in the peak shape reflecting the difference in the W coordination environment (i.e., tetrahedral in $Bi_{14}WO_{24}$ versus octahedral in Bi_2WO_6). While the W L_3 absorption edge of $Bi_{14}WO_{24}$ (tetrahedral) appears to be a single peak, Bi_2WO_6 (octahedral) clearly shows two overlapping peaks (the difference between the two is more obvious in the first derivative plot – inset of Figure 8). This difference is attributed to the smaller ligand field splitting of the W 5d orbitals in the tetrahedral environment than the

octahedral environment [29]. Therefore, the second peak in the derivative plot (~10211 eV, as indicated by the arrow) is a 'fingerprint' of W^{6+} occupying an octahedral site. Based on the XANES spectra shown in Figure 8 (especially the inset), the W^{6+} ions are located predominantly at octahedral sites in W6 whereas the local environment in W3 is mixed (i.e., both octahedral and tetrahedral sites). The amount of octahedral sites occupied by W^{6+} increases with increasing W content in the samples: W3 < W4 < W4.5 < W5 < W6 (essentially pure octahedral sites). These XANES results are in good agreement with the results presented in earlier sections.

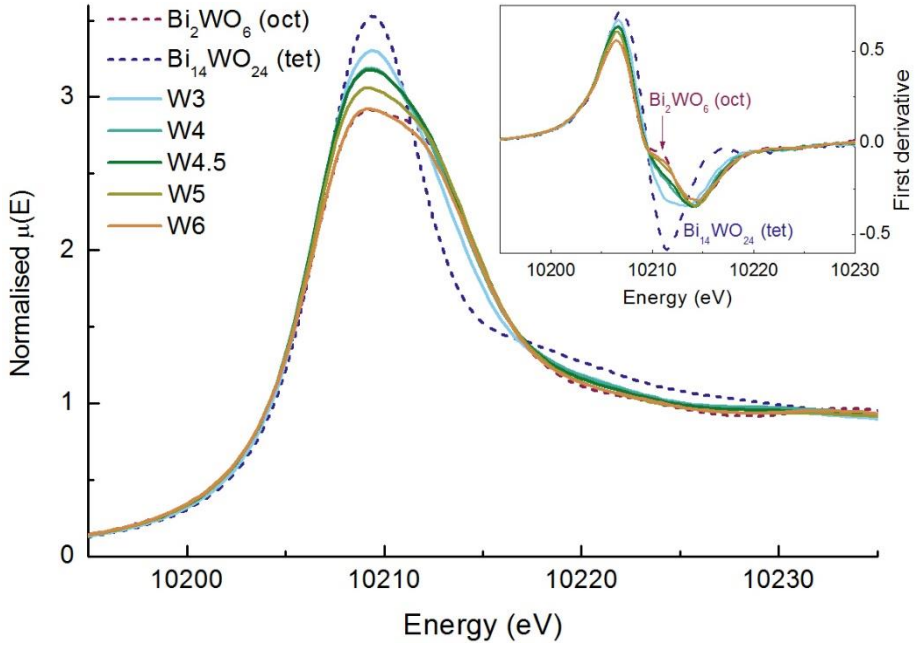

Figure 8. Normalised W L_3 edge XANES spectra obtained from W3 ($Bi_{24}W_3O_{45}$), W4 ($Bi_{23}W_4O_{46.5}$), W4.5 ($Bi_{22.5}W_{4.5}O_{47.25}$), W5 ($Bi_{22}W_5O_{48}$), W6 ($Bi_{21}W_6O_{49.5}$) and $Bi_{14}W^{6+}O_{24}$ (tetrahedral) (dash blue curve) and $Bi_2W^{6+}O_6$ (octahedral) (dash red curve) standards.

3.4 Impedance measurements

At low temperatures, about half of a large semi-circle arc at high frequencies, and a Warburg-type electrode response at low frequencies were observed in the complex impedance plot. The capacitance at 400°C for the semi-circle arc was estimated using $\omega RC = 1$ ($\omega = 2\pi f_{max}$, where f_{max} is the frequency at the maximum imaginary impedance, Z''_{max}, for the semicircular arc) and is 11.2 pF cm^{-1} for W4 (11.9 pF cm^{-1} for W5), consistent with a bulk response. At higher temperatures, the high frequency semi-circle disappears and positive values for Z'' at higher frequencies are obtained. High frequency intercepts were estimated as the total resistivities of the sample.

Figure 9 shows the Arrhenius plots for W4 (W5 shows similar behaviour). A significant decrease in gradient, indicating a lowering of the activation energy for oxide ion migration,

was observed around 800°C, corresponding to the transition from tetragonal type Ib to cubic type II phase. Above 800°C, conductivities were stable during thermal cycling; while below 800°C a slight decrease in conductivity was observed after the first cycle, with conductivities being stable in the subsequent two cycles. This is consistent with a decrease in conductivity due to oxygen sublattice ordering on transition from the rather disordered cubic type II phase to the comparably ordered type Ib phase. Lab-XRD of the samples after the impedance measurement confirmed tetragonal type Ib phase ($I4_1$, a = 12.5201 Å, c = 11.2582 Å for W4).

The Arrhenius plot gave activation energies of 1.05 eV below (after 2nd cycle) and 0.42 eV above 800°C, corresponding to activation energies for oxygen mobility in the type Ib and type II phase respectively. Conductivities are comparable to those of the type II phase in the Bi-Nb-O system [31] and essentially the same as those of yttria-stabilised zirconia [32] over the lifetime of the experiment (Figure 9).

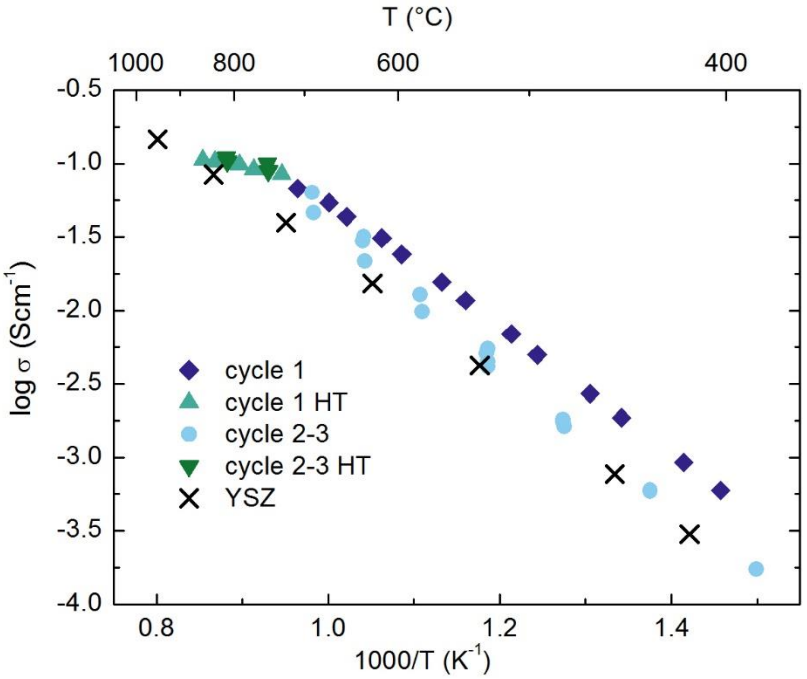

Figure 9: Arrhenius plot for several heating & cooling cycles for $Bi_{23}W_4O_{46.5}$ compared to yttria-stabilised zirconia (YSZ).

4. Conclusions

Our experimental results confirm that the solid solution of cubic type II $Bi_{1-x}W_xO_{1.5+1.5x}$ extends from x = 0.148 to x = 0.185. This is in perfect agreement with previously published results from single crystal investigations and *ab initio* computational simulations [11]. Throughout the solid solution range, the type II phase can only be stabilised down to room temperature by quenching (Bi-rich samples) or relatively high cooling rates (W-rich samples). Lower cooling rates yield the type Ib phase (Bi-rich samples) or a mixture of type Ib and Aurivillius phase

(W-rich samples). The stability of the type II phase increases with increasing tungsten content to the upper limit of the solid solution range at a composition of $Bi_{22}W_5O_{48}$, i.e., full occupancy of W on the Bi4 site. S-XRD patterns of Bi-rich samples show significant peak broadening, indicating strain in the structure due to the large size of Bi^{3+} ions. Although the average structure of the type II phase can be approximately described within a 3×3×3 supercell of the simple cubic δ-Bi_2O_3 unit cell (i.e., a commensurate modulation vector of ε = 1/3) the actual structure exhibits (3+3)-dimensional incommensurate modulations throughout the solid solution range ($0.317 \leq \varepsilon \leq 0.321$). Analysis of the W L_3 edge across the solid solution confirms the oxidation state of W^{6+} and the increase of octahedral sites occupied by W^{6+} with increasing W content. The oxide ionic conductivity of $Bi_{23}W_4O_{46.5}$ is comparable to YSZ. Due to transformation to the tetragonal Ib phase, a decrease in ionic conductivity on thermal cycling of approximately half an order of magnitude is observed.

Acknowledgments

This work was supported by Australian Research Council grant DP150102863, a Royal Society *International Exchanges* grant, and the Australian Institute for Nuclear Science and Engineering (AINSE Postgraduate Research Award for JW). Work at the Australian Synchrotron was performed with the assistance of Justin Kimpton at the powder diffraction beamline and Peter Kappen at the XAS beamline. Maxim Avdeev assisted with NPD data collections at the ACNS.

References

1 Hull, S., Norberg, S. T., Tucker, M. G., Eriksson, S. G., Mohn, C. E. & Stolen, S. Neutron total scattering study of the δ and β phases of Bi_2O_3. *Dalton transactions*, 8737-8745, doi:10.1039/b910484b (2009).

2 Battle, P. D., Catlow, C. R. A., Drennan, J. & Murray, A. D. The Structural-Properties of the Oxygen Conducting δ Phase of Bi_2O_3. *J Phys C Solid State* **16**, L561-L566, doi:10.1088/0022-3719/16/17/003 (1983).

3 Gattow, G. & Schröder, H. Über Wismutoxide. III. Die Kristallstruktur der Hochtemperaturmodifikation von Wismut(III)-oxid (δ-Bi_2O_3). *Zeitschrift für anorganische und allgemeine Chemie* **318**, 176-189, doi:10.1002/zaac.19623180307 (1962).

4 Ling, C. D., Schmid, S., Blanchard, P. E., Petricek, V., McIntyre, G. J., Sharma, N., Maljuk, A., Yaremchenko, A. A., Kharton, V. V., Gutmann, M. & Withers, R. L. A (3 + 3)-dimensional "hypercubic" oxide-ionic conductor: type II Bi_2O_3-Nb_2O_5. *Journal of the American Chemical Society* **135**, 6477-6484, doi:10.1021/ja3109328 (2013).

5 Struzik, M., Malys, M., Wrobel, W., Abrahams, I., Krok, F. & Dygas, J. R. Ordered fluorite phases in the Bi_2O_3-Ta_2O_5 system: A structural and electrical investigation. *Solid State Ionics* **202**, 22-29, doi:10.1016/j.ssi.2011.08.009 (2011).

6 Esmaeilzadeh, S. 3-dimensional modulations in bismuth oxide based compounds with average fluorite type structures. *Ferroelectrics* **250**, 63-66, doi:10.1080/00150190108225033 (2001).

7 Esmaeilzadeh, S., Lundgren, S., Hålenius, U. & Grins, J. $Bi_{1-x}Cr_xO_{1.5+1.5x}$, $0.05 \leq x \leq 0.15$: A New High-Temperature Solid Solution with a Three-Dimensional Incommensurate Modulation. *Journal of Solid State Chemistry* **156**, 168-180, doi:10.1006/jssc.2000.8978 (2001).

8 Valldor, M., Esmaeilzadeh, S., Pay-Gomez, C. & Grins, J. A New High-Temperature Cubic Fluorite-Type Phase $Mo_{0.16}Bi_{0.84}O_{1.74}$ with a Rare Three-Dimensional Incommensurate Modulation. *Journal of Solid State Chemistry* **152**, 573-576, doi:10.1006/jssc.2000.8742 (2000).

9 Ling, C. D., Withers, R. L., Schmid, S. & Thompson, J. G. A Review of Bismuth-Rich Binary Oxides in the Systems Bi_2O_3–Nb_2O_5, Bi_2O_3–Ta_2O_5, Bi_2O_3–MoO_3, and Bi_2O_3–WO_3. *Journal of Solid State Chemistry* **137**, 42-61, doi:10.1006/jssc.1997.7677 (1998).

10 Withers, R. L., Ling, C. D. & Schmid, S. Atomic Modulation Functions, Periodic Nodal Surfaces and the three-dimensional incommensurately modulated $(1\text{-}x)Bi_2O_3 \cdot xNb_2O_5$, $0.06 < x < 0.23$, solid solution. *Zeitschrift Fur Kristallographie* **214**, 296-304, doi:10.1524/zkri.1999.214.5.296 (1999).

11 Wind, J., Auckett, J. E., Withers, R. L., Piltz, R. O., Maljuk, A. & Ling, C. D. Type II $Bi_{1-x}W_xO_{1.5+1.5x}$: a (3 + 3)-dimensional commensurate modulation that stabilizes the fast-ion conducting delta phase of bismuth oxide. *Acta crystallographica. Section B, Structural science* **71**, 679-687, doi:10.1107/S2052520615018351 (2015).

12 Sharma, N., Macquart, R. B., Avdeev, M., Christensen, M., McIntyre, G. J., Chen, Y. S. & Ling, C. D. Re-investigation of the structure and crystal chemistry of the Bi_2O_3-W_2O_6 'type (Ib)' solid solution using single-crystal neutron and synchrotron X-ray diffraction. *Acta crystallographica. Section B, Structural science* **66**, 165-172, doi:10.1107/S0108768110001874 (2010).

13 Watanabe, A. & Ono, A. Thermostable region of an oxide ion conductor, $Bi_7WO_{13.5}$ ($=7Bi_2O_3xWO_3$), and the solid solubility extension. *Solid State Ionics* **174**, 15-18, doi:10.1016/j.ssi.2004.04.039 (2004).

14 Nespolo, M., Watanabe, A. & Suetsugu, Y. Re-Investigation of the Structure of $7Bi_2O_3 \cdot 2WO_3$ by Single-Crystal X-ray Diffraction. *Crystal Research and Technology* **37**, 414-422, doi:10.1002/1521-4079(200204)37:4<414::aid-crat414>3.0.co;2-d (2002).

15 Zhou, W. Defect Fluorite Superstructures in the Bi_2O_3-WO_3 System. *Journal of Solid State Chemistry* **108**, 381-394, doi:10.1006/jssc.1994.1056 (1994).

16 Watanabe, A., Ishizawa, N. & Kato, M. An outline of the stucture of $7Bi_2O_3 \cdot 2WO_3$ and its solid solutions. *Journal of Solid State Chemistry* **60**, 252-257, doi:10.1016/0022-4596(85)90119-7 (1985).

17 Knight, K. S. The Crystal-Structure of Russellite - a Redetermination Using Neutron Powder Diffraction of Synthetic Bi_2WO_6. *Mineral Mag* **56**, 399-409, doi:10.1180/minmag.1992.056.384.13 (1992).

18 Rae, A. D., Thompson, J. G. & Withers, R. L. Structure Refinement of Commensurately Modulated Bismuth Tungstate, Bi_2WO_6. *Acta Crystallographica Section B-Structural Science* **47**, 870-881, doi:10.1107/S0108768191008030 (1991).

19 Wallwork, K. S., Kennedy, B. J. & Wang, D. The High Resolution Powder Diffraction Beamline for the Australian Synchrotron. **879**, 879-882, doi:10.1063/1.2436201 (2007).

20 Liss, K.-D., Hunter, B., Hagen, M., Noakes, T. & Kennedy, S. Echidna—the new high-resolution powder diffractometer being built at OPAL. *Physica B: Condensed Matter* **385-386**, 1010-1012, doi:10.1016/j.physb.2006.05.322 (2006).

21 Toby, B. H. EXPGUI, a graphical user interface for GSAS. *Journal of Applied Crystallography* **34**, 210-213, doi:10.1107/S0021889801002242 (2001).
22 Petříček, V., Dušek, M. & Palatinus, L. Crystallographic Computing System JANA2006: General features. *Zeitschrift für Kristallographie - Crystalline Materials* **229**, doi:10.1515/zkri-2014-1737 (2014).
23 Glover, C., McKinlay, J., Clift, M., Barg, B., Boldeman, J., Ridgway, M., Foran, G., Garrett, R., Lay, P. & Broadbent, A. Status of the x-ray absorption spectroscopy (XAS) beamline at the Australian synchrotron. *Aip Conf Proc* **882**, 884-886, doi:10.1063/1.2644692 (2007).
24 Ravel, B. & Newville, M. ATHENA, ARTEMIS, HEPHAESTUS: data analysis for X-ray absorption spectroscopy using IFEFFIT. *J Synchrotron Radiat* **12**, 537-541, doi:10.1107/S0909049505012719 (2005).
25 Zhang, Z., Avdeev, M., de los Reyes, M., Lumpkin, G. R., Kennedy, B. J., Blanchard, P. E. R., Liu, S., Tadich, A. & Cowie, B. C. C. Probing Long- and Short-Range Disorder in $Y_2Ti_{2-x}Hf_xO_7$ by Diffraction and Spectroscopy Techniques. *The Journal of Physical Chemistry C* **120**, 26465-26479, doi:10.1021/acs.jpcc.6b07076 (2016).
26 Zhang, Z., Middleburgh, S. C., de los Reyes, M., Lumpkin, G. R., Kennedy, B. J., Blanchard, P. E. R., Reynolds, E. & Jang, L.-Y. Gradual Structural Evolution from Pyrochlore to Defect-Fluorite in $Y_2Sn_{2-x}Zr_xO_7$: Average vs Local Structure. *The Journal of Physical Chemistry C* **117**, 26740-26749, doi:10.1021/jp408682r (2013).
27 Crumpton, T. E., Francesconi, M. G. & Greaves, C. The structural chemistry of $Bi_{14}MO_{24}$ (M=Cr, Mo, W) phases: bismuth oxides containing discrete MO_4 tetrahedra. *Journal of Solid State Chemistry* **175**, 197-206, doi:10.1016/s0022-4596(03)00246-9 (2003).
28 Ling, C. D., Withers, R. L., Thompson, J. G. & Schmid, S. Structures of $Bi_{14}WO_{24}$ and $Bi_{14}MoO_{24}$ from neutron powder diffraction data. *Acta Crystallographica Section B: Structural Science* **55**, 306-312, doi:10.1107/S0108768198014086 (1999).
29 Yamazoe, S., Hitomi, Y., Shishido, T. & Tanaka, T. XAFS Study of Tungsten L_1- and L_3-Edges: Structural Analysis of WO_3 Species Loaded on TiO_2 as a Catalyst for Photo-oxidation of NH_3. *The Journal of Physical Chemistry C* **112**, 6869-6879, doi:10.1021/jp711250f (2008).
30 Kuzmin, A., Purans, J. & Kalendarev, R. Local structure and vibrational dynamics in $NiWO_4$. *Ferroelectrics* **258**, 21-30, doi:10.1080/00150190108008653 (2001).
31 Tate, M. L., Hack, J., Kuang, X., McIntyre, G. J., Withers, R. L., Johnson, M. R. & Radosavljevic Evans, I. $Bi_{1-x}Nb_xO_{1.5+x}$ (x=0.0625, 0.12) fast ion conductors: Structures, stability and oxide ion migration pathways. *Journal of Solid State Chemistry* **225**, 383-390, doi:10.1016/j.jssc.2015.01.006 (2015).
32 Kharton, V., Marques, F. & Atkinson, A. Transport properties of solid oxide electrolyte ceramics: a brief review. *Solid State Ionics* **174**, 135-149, doi:10.1016/j.ssi.2004.06.015 (2004).